As-grown Suspended Carbon Nanotubes

Fabrication and Electronic Characterization of Ultra Clean Suspended As-grown Single Walled Carbon Nanotubes

Daniel Steffensen

Supervisors:
Jesper Nygård
Kasper Grove Rasmussen
Morten Canth Hels

June 9, 2015

Daniel Steffensen
Kapelvej 46
2200 Copenhagen N
Denmark
22 21 77 87
steffensen.d@hotmail.com
pnv234@ku.dk

The work concerning the fabrication and characterization of ultra-clean suspended as-grown single-walled carbon nanotubes (SWNT) that is the focus of my bachelor project, and will be presented in this thesis. The fabrication that concerns finding the right metal stacking combination for the contacts implement these and define the cleanliness through measurements.
The contacts were variations of a sticking layer of either Ta or W with an adhesion layer of Pt on top. The SWNTs were grown by chemical vapor deposition, followed by characterization of these at room temperature. The energy spectra were determined at sub-kelvin temperatures (T$\sim$300mK) in a cryostat by confining the SWNT as quantum dots (QDs).
The obtained devices showed Coulomb blockade (CB) and Kondo effects. Through analysis, however, it was shown that the structures were highly irregular, suggesting multiple interacting ill-defined QDs, most likely produced by the irregular contacts after growth. A short outlook will be given for further development of clean devices.

Contents

1 Introduction

Ever since Sumio Iijima discovered carbon nanotubes (CNT) in 1991, they have been of great interest for multiple applications, such as field emission displays, light sources, actuators, sensors and batteries[1]. The vast application possibilities are due to the fascinating physical and electronic structure of CNTs.
This thesis will concern the application of CNTs in nano electronic devices. Traditionally, such devices are fabricated by depositing CNTs on either a substrate, followed by alignment of electrodes on top, or by deposition on predefined contacts. Such fabrication procedures are not ideal in the way that the tube interacts with the substrate (by van der Waals interactions). To prevent this, suspended tubes have been fabricated by etching the substrate between two electrodes which generates a trench[2].
However, to obtain ultra clean devices, the growth of the tubes should be the last step, because it prevents interactions with substrate, electron beams or solvents[3], keeping them intact, so-called as-grown. A perfect as-grown ultra clean suspended carbon nanotube should be suspended on top of two well- and predefined electrodes, only surrounded by the ambient atmosphere.
The work in this thesis will concern the fabrication of such devices, based on previous studies [4][5][6] and characterization of these devices both through Quantum Dots (QD) measurements and through scanning electron microscopy (SEM). If such ultra-clean suspended devices are to be obtained, the study might be taken for further application for more complicated devices such as Cooper pair splitters[7].
The outline of this thesis will be a short introduction of CNTs and QDs, followed by the fabrication procedure used to obtain the devices. The samples will be cooled down to cryogenic temperatures ($T < 1K$) to investigate the quantum mechanical behavior[1] of the CNTs as QDs. Hopefully, they will obtain a regular energy spectrum, convincing the cleanliness of the tubes. Lastly, an analysis and discussion of the obtained devices will be presented and a further outlook will be proposed.

2 Carbon Nanotubes

In order to understand, investigate and optimize single-wall carbon nanotubes (SWCNT), one must understand their physical and electronic structure.

2.1 Physical Structure

Take a two-dimensional honeycomb graphene sheet, roll it up and you have a CNT. The number of ways to roll a graphene sheet is infinite, hence the number of structures are equally infinite. In order to differentiate the structures a chiral vector $\mathbf{C}$ is ascribed to each roll-up. This vector connects the two lattice points to be superposed in the roll-up (the circumference), see Fig.1(a). $\mathbf{C}$ is defined in the basis of the lattice

[1] The discrete energy levels of the CNT as a QD can be explained through the well known 'Particle in a box'[8], and thus the energies increase with decreasing sample length. For the quantum levels to be detectable the energies has to overrule the thermal energy $k_B T$[9]. So by achieving a small sample, and cryogenic temperatures these energy levels should be observable.

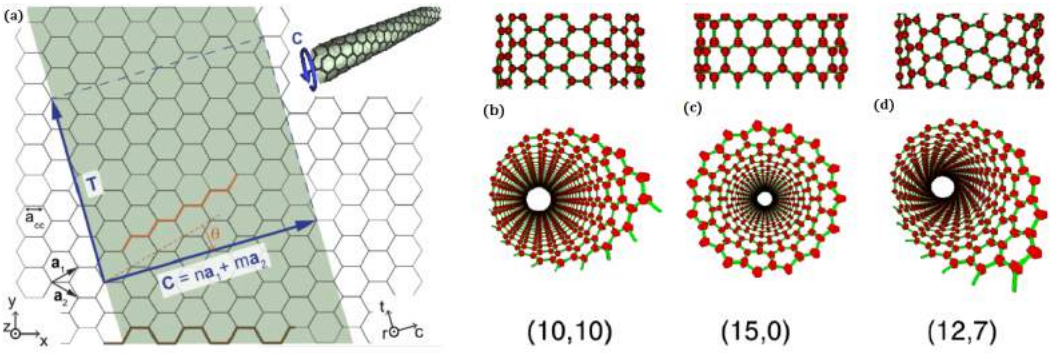

Figure 1: Structure of CNT. (a) The sheet of graphene to be rolled-up (shaded area). The unit cell of the tube is the parallelogram spanned by the chiral vector $\mathbf{C}$, and the translation vector $\mathbf{T}$. Also, the atomic distance $\mathbf{a}_{CC}$, the basis lattice vectors $\mathbf{a}_1$ and $\mathbf{a}_2$, the chiral angle θ and the two coordinate systems for the graphene (x, y, z) and for the tube (c, t, r), are visible in the figure from [10]. (b) Examples of the three classifications of CNT: armchair $(n = m)$, zig-zag $(m = 0)$ and chiral. The three classifications can be seen in (a) by the colored lines: brown, red and blue, respectively. From [11].

vectors $\mathbf{a}_1$ and $\mathbf{a}_2$, in the way:

$$\mathbf{C} = n\mathbf{a}_1 + m\mathbf{a}_2. \tag{1}$$

Usually the indices (n, m) are given, instead of the chiral vector. Some restrictions must be given to these indices, in order to prevent different labels for the same structure; $-n/2 < m \leq n$. Some prefer to label the structures by the diameter D, and the angle θ between $\mathbf{C}$ and $\mathbf{a}_1$, called the chiral angle.
Furthermore, the tubes are classified as either zig-zag $(m = 0)$, armchair $(n = m)$ or just chiral for all other cases, see Fig.1(b).

2.2 Electronic Structure

From quantum mechanical calculations, it is knwon that the electronic configuration of carbon is $1s^2 2s^2 2p^2$[8]. The orbitals in the outermost shell, $n = 2$, undergo a sp^2 hybridization[2], which again hybridizes with neighboring carbon atoms. These hybridizations form bonding σ-, and anti-bonding σ*-bands, generating the three covalent bonds per atom. Furthermore, unhybridized p_z orbitals also create bonding π-, and anti-bonding π*-bands with neighbors[10].
Now, if the electrons are then filled in, with respect to the Pauli principle, we should end up with a full σ-band (three electrons), and a full π-band (one electron), leaving the Fermi energy ϵ_F just in the middle of the π- and π*-band, which gives a semi-metal, and π* is thus the conducting band.
The next step is to take the unit cell of graphene and transform it into k-space, and find the first Brillouin zone. The 3D band structure can then be calculated by the tight binding approximation[12], and plotted in k-space. See Fig.2.

[2] An admixture of $2s$, $2p_x$ and $2p_y$ orbitals.

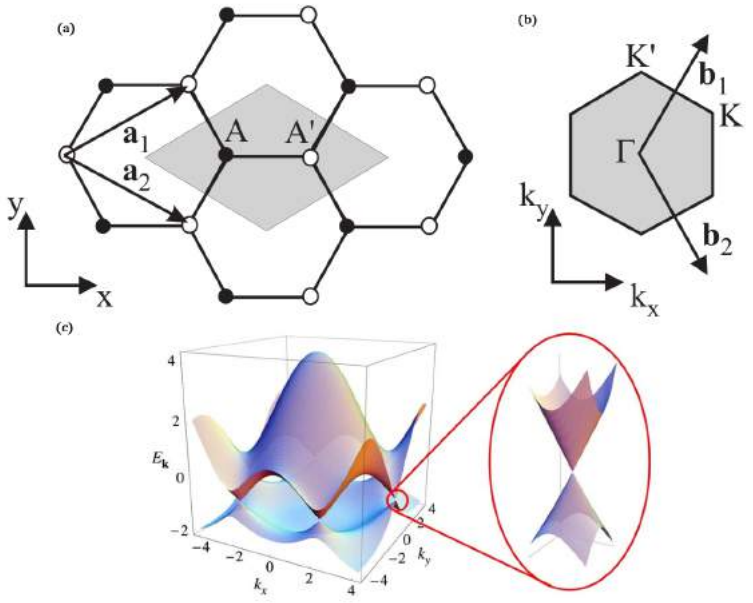

Figure 2: Graphene in k-space: (a) Unit cell of graphene (shaded area), with the inequivalent carbon atoms (white A' and black A). The cell is spanned by the unit vectors $\mathbf{a}_1$ and $\mathbf{a}_2$. (b) Graphene in k-space with the first Brillouin Zone (shaded), and the two reciprocal vectors $\mathbf{b}_1$ and $\mathbf{b}_2$. The two inequivalent corner points, by Bloch's Theorem, are also illustrated (K, and K') from [13]. (c) Three dimensional dispersion relation, from tight binding approximation, of graphene. The Fermi energy is exactly where the Dirac cones intersect and is set to zero. Only the π-orbitals are shown, from [12].

As seen from Fig.2(c), the Fermi energy is set to zero and is exactly where the cones touch, showing that the upper band must be the conducting π*-band, and the lower must be the valence π-band as predicted.
The electrons in the band are described by a Bloch wavefunction:

$$\psi_{\mathbf{k}}(\mathbf{r}) = u_{\mathbf{k}}(\mathbf{r})\mathrm{e}^{i\mathbf{k}\cdot\mathbf{r}}, \tag{2}$$

with $u_{\mathbf{k}}(\mathbf{r}) = u_{\mathbf{k}}(\mathbf{r}+\mathbf{C})$ as the period of the potential, in order to include the electrons Coulomb interaction with the ion cores[14]. Points connected by a reciprocal vector must be the equivalent and hence the nomenclature in Fig.2(b) of K and K'. These points are also known as Dirac points, and are exactly where the (Dirac)-cones touch in Fig.2(c).
When the sheet is rolled-up (assuming that the diameter D of the tube is larger than the atomic distance $\mathbf{a}_{CC}$, leaving the band structure unperturbed) periodic boundary conditions must occur in the direction of $\mathbf{C}$, giving;

$$\mathbf{C}\cdot\mathbf{k} = 2\pi q \tag{3}$$

with q as an integer, and $\mathbf{k}$ as the wave vector. These conditions give quantized lines

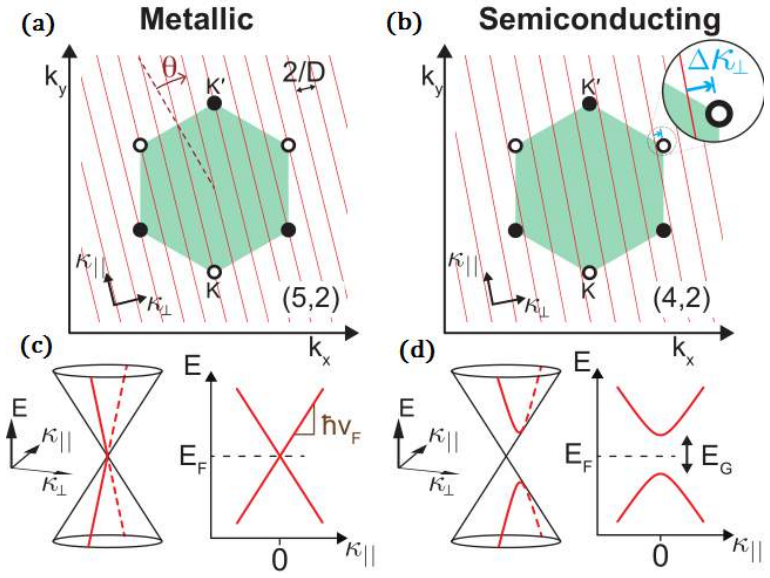

Figure 3: Band structure of CNT for: (a) with the quantization lines intersecting the Dirac-cones, allowing states at the Fermi energy ϵ_F which generates a metallic tube (c), and (b) where the lines are displaced by $\Delta\kappa_\perp$, allowing no states at the ϵ_F, which gives a semi conducting CNT, from [10].

in **k**-space, since $\mathbf{k}_\parallel$ can take all values, when assuming an infinite tube, giving the allowed **k** values, see Fig.3.
From the allowed **k**-values and the 3D dispersion relation for graphene in Fig.2, it is possible to determine the band structure of a CNT. See Fig.3(a) where the quantization lines exactly intersect the Dirac points, allowing **k**-values at the Fermi energy, which generates a metallic CNT, Fig3(c). Whereas in Fig.3(b), where the lines do not intersect the Dirac points there are no allowed k-vectors at the Fermi energy, which generates a band gap. Thus the giving tube is semiconducting (Fig.3(d)). A third kind of tubes are observed with a very narrow band gap induced by the curvature of the CNT, which displaces the Dirac points.
Notice that we are only concerned with the states around ϵ_F, since the electrons are fermions and are distributed with respect to the Fermi-Dirac distribution:

$$f_0(\epsilon) = \frac{1}{\mathrm{e}^{\frac{\epsilon-\mu}{k_B T}} + 1}, \tag{4}$$

and only states in a range of $k_B T$ can be excited to the conducting band. Here k_B is the Boltzmann constant, T is the temperature and μ is the chemical potential[15].

3 Mesoscopic Transport in Carbon Nanotubes

Before starting the analysis, the concept of electron transport in mesoscopic structures needs to be understood. So in this section the CNTs will first briefly be described as one dimensional wires, and afterwards as confined QDs. The importance of the 1D behavior is essential in determining the cleanliness of the devices.

3.1 One Dimensional Wire

Normally one would expect that the resistance would approach zero, as the length of the wire approaches zero. However, this is shown through experiments not to be true[16]. This is basically because of the limited number of modes in the 1D wire compared to the connected contacts. This proves that the resistance in this limit is

$$G^{-1} = \frac{h}{e^2 M}, \tag{5}$$

with h as the Planck constant, e the elementary charge and M as the number of modes, assumed reflection-less contacts. Due to spin and valley quantum number (K and K') each energy level of a CNT is four times degenerated. For a more thorough description see [5][16].

3.2 Coulomb Blockade

When confining the tube as a zero dimensional QD, the electrons can be considered through the well known 'particle in a box' potential with discrete energy levels. These levels resemble that of an atom, and therefore QDs are often thought of as artificial atoms[17].
To understand the exact energy spectra is a theoretically complicated procedure, and some approximations must be done: all Coulomb interactions are parametrized into one single capacitance $\mathrm{C} = \mathrm{C}_s + \mathrm{C}_d + \mathrm{C}_g$, with C_s, C_d and C_g as the capacitances of the source, drain and backgate contacts respectively. Second, the energy levels of the dot are not perturbated by the capacitance C, nor by the number of electrons on the dot. These approximations are collectively called 'The Constant Interaction Model' [18]. Through this model the whole experimental setup[3] can be explained in a simple manner with the diagram in Fig.4(a).
The energy of the dot is defined in the usual way for a classical capacitor; $U = \frac{Q}{2C}$. Here C is the total capacitance, and Q the charge of the dot. This charge has a discrete part: the charges from the added electrons, $-|e|(N - N_0)$, where N_0 is the natural number of electrons on the dot, and also a continuous part: charges produced by the capacitive couplings.
From the previous sections, it is also known that CNTs have discrete confined quantum energy levels E_n, which also needs to be added;

$$U(N) = \frac{[-|e|(N - N_0) + C_S V_S + C_D V_D + C_G V_G]^2}{2C} + \sum_{n=1}^{N} E_n. \tag{6}$$

Again we will turn to the Fermi-Dirac distribution (eq.(4)), and since $T \to 0$ in the given experiment for QD, the Fermi energy can be approximated as the chemical potential μ, often referred to as the Fermi level in semiconducting physics. In this approach a potential landscape is often conventional, and gives an intuitive understanding of the electron transport, see Fig.4.

[3] To be discussed in Section.5.2.

The electrochemical potential of the dot is usually defined as the energy to add the last electron(from eq.(6)):

$$\mu_N \equiv U(N) - U(N-1) \tag{7}$$

$$= (N - N_0 - \frac{1}{2})E_C - \frac{E_C}{|e|}(C_S V_S + C_D V_D + C_G V_G) + E_N, \tag{8}$$

with $E_C = \frac{e^2}{C}$, as the charging energy. The spacing between successive electrochemical potentials must then be:

$$\mu_{N+1} - \mu_N = E_C + \Delta E \tag{9}$$

$$= E_{add}, \tag{10}$$

called the addition energy, with ΔE as the energy difference between the confined quantum levels. For degenerate levels $\Delta E = 0$, until the level is totally filled.
If we then go back to Fig.4, it is clear that the N+1'th electrochemical level of the dot has to be in the bias window, in order for single electrons transport (SET) to occur (Fig.4(c)). The bias window is spanned by the electrochemical of the source and drain contacts, μ_S and μ_D respectively. Whenever μ_{N+1} is not in the bias window, no current flows, Fig.4(b), this phenomena is called Coulomb blockade (QB).

3.3 Energy Scales

For CB to occur, the QD has to be an isolated system. As stated earlier it is assumed that $T \sim 0$, in order to prevent thermal charging, and thus

$$k_B T << E_C. \tag{11}$$

To prevent quantum fluctuations of electrons on and off the dot the uncertainty of the energy must be less than the charging energy barrier $\Delta\epsilon << E_C$. If it is assumed that quantum fluctuations can be approximated by the Heisenberg uncertainty principle, and that the charge time $\Delta t = R_t C$, with $R_t = R_s + R_d$, the relation becomes:

$$\Delta\epsilon \Delta t \sim h \tag{12}$$

$$\Delta\epsilon \sim \frac{h}{R_t C}$$

$$E_C >> \frac{h}{R_t C}$$

$$\Downarrow$$

$$R_t > \frac{h}{e^2}. \tag{13}$$

Lastly, the bias window has to be sufficiently small, in order to allow only one electrochemical state:

$$-|e|V_{SD} < E_C \tag{14}$$

Notice that if these condition are not met Fabry-Perot effects, Kondo physics and excited states may occur [10][13].

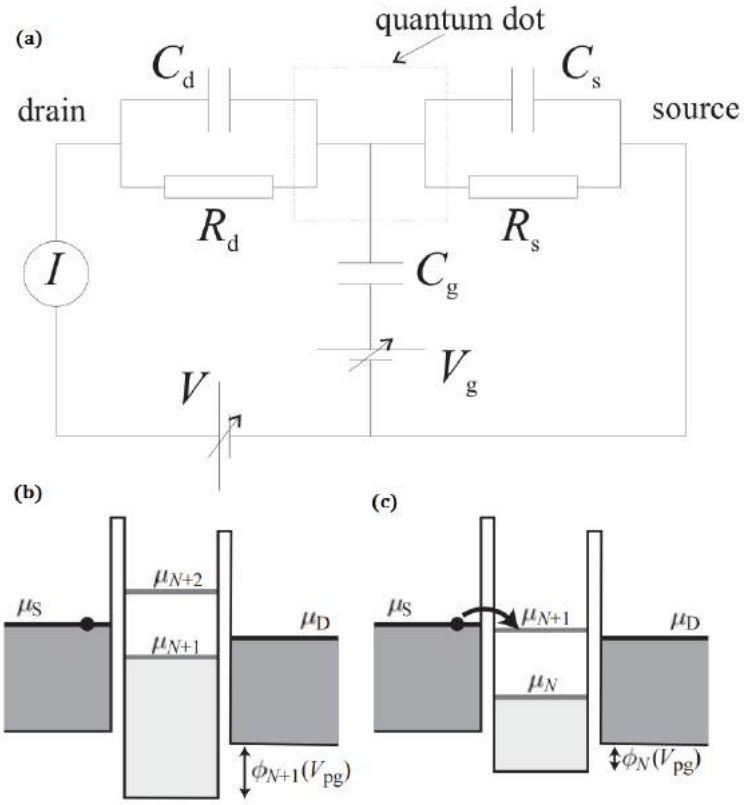

Figure 4: The constant interaction model: (a) A schematic illustration of the model described in the section. All electromagnetic forces are parameterized into $C = C_s + C_d + C_g$, and the tunneling barriers as the resistances R_s and R_d, from [13]. (b) Potential landscape of the Fermi levels of the QD. Since there is no level in the bias window, no electron transport can occur. This is called Coulomb blockade. (c) Here the level of the dot is in the bias window, which allows single electron transport (SET). The levels of the dot can be adjusted capacitive by the gate voltage, from [19].

3.4 Bias Spectroscopy

Bias spectroscopy, or often referred to as diamond plots (due to the diamond shaped areas, see Fig.12) is a great tool for determination of the different energies.
Consider Fig.5. where the black lines indicate alignment of the chemical potentials of the dot with μ_S or μ_D. For $-|e|V_{SD} = 0$ simple illustrate points with SET, and lines with CB along the V_g axis. When $-|e|V_{SD}$ is increased the dot enters high bias regime and new excited states become visible. The yellow and blue lines in the figure indicate alignment of excited electrochemical potentials with either μ_S or μ_D. It is clear that μ_{dot} changes as a function of V_{SD}. From this figure the different capacitive couplings can be derived in the way; $\frac{d(V_{SD})}{dV_g} = \frac{C_G}{C_S}$ for the positive slope, and $\frac{-C_G}{C-C_S}$ for the negative slope (from the sides of the Coulomb diamonds)[18]. For a more intuitive understanding of the different lines see the small potential landscapes in the figure.

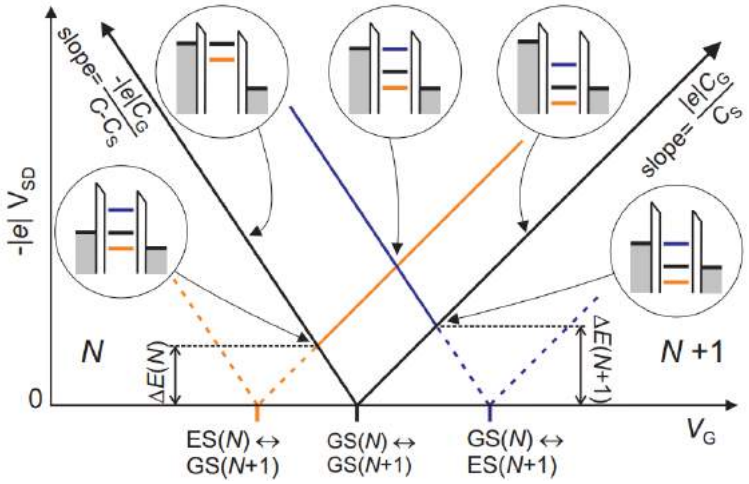

Figure 5: Schematic illustration of a bias spectrum. With lines indicating different alignments of different states (blue and yellow are excited states). For a better understanding small insets of schematic diagrams are included, from [18]. The capacitive couplings are derived through the slopes of the diamond's sides. Notice that the notation of energy is different in this figure, compared to the definition used in this thesis. Lastly ES stands for excited state, and GS for ground state. N is the number of electrons in the giving state.

A bias sweep is usually plotted with differential conductance[4] as a function of both V_g and V_{SD}. In such two dimensional plots the diamonds are regions with CB, and the colored areas are regions with electrons transport. For a constant V_g, the height of the diamond must be the energy difference between two levels on the dot, since this is the maximum bias voltage before current can flow.

4 Device Fabrication and Growth

To obtain a CNT and measure its characteristics firstly a substrate, on which the tubes can be grown onto has to be prepared. The geometry of such samples is typically in the sub-micron range to bring the quantum mechanical behavior into play.

To obtain this, the fabrication can be divided into five general steps:

1. Sample preparation.
2. Defining contacts by electron beam lithography (EBL), development and ashing.
3. Metal sputtering and/or evaporation on pattern followed by lift-off.
4. EBL to define the catalyst islands, followed by development.
5. Applying catalyst to the island, and lift-off.
6. Growth of CNTs in chemical vapor deposition(CVD) furnace.
7. Bonding to a chip carrier.

[4]Due to the nonlinear behavior of CNTs as QDs. To be discussed in Section.5.2.

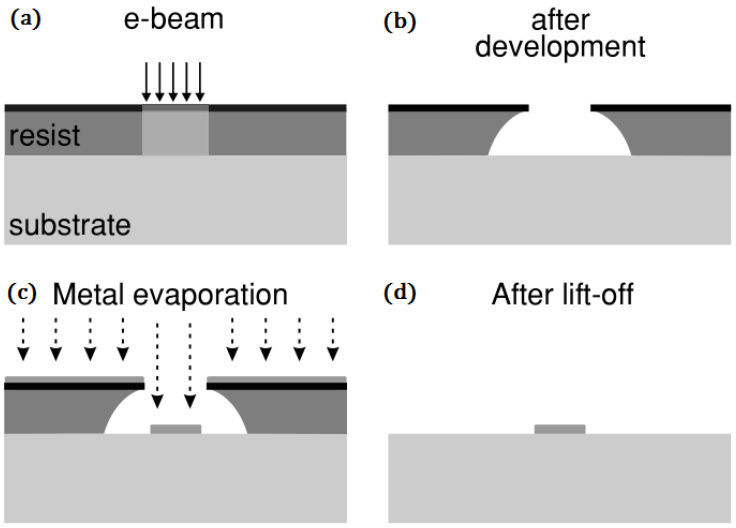

Figure 6: Basic steps in definition of metal patterns by electron beam lithography an lift-off, from [20].

Due to the short time basis of this project, only steps 5-7 were done by the author[5], but some remarks about earlier steps also need consideration. For a brief presentation of the previous steps see Fig.6.

4.1 General Considerations

Since the tubes are randomly scattered when grown in the CVD furnace, the geometry of the contacts need to optimize the chances of a single suspended tube, but not multiple tubes. To do this the geometry in Fig.7(d) was chosen, with 300 nm distance between neighboring contacts of width 500 nm.
Because of the harsh environment under growth ($T = 910\,^{\circ}\mathrm{C}$), the metal contacts need to be made of specific materials to prevent the contacts from melting, alloying and irregularities. Based on previous studies[6][5][4] the metal contacts were made with a sticking layer of Ta or W and an adhesion Pt layer on top. For development and outcome of samples (generations) see section.4.5. To distinguish different samples from each other, they are ascribed a generation number, i.e. first generation is called gen1 etc.

4.2 Applying Catalyst

This step can be done in various ways, naturally leading one to various results[6], and therefore we decided to use just one procedure consistently throughout the project. After the patterns for the catalyst islands are defined by EBL, the sample is developed: 55 seconds in MIBK (Methylisobutylketon) (diluted with IPA 1:3), then 55 seconds in IPA (Isopropanol). The sample was moved in circles to generate flow in the solutions. The catalyst, $Fe(NO_3)_3{\cdot}9H_2O$, was then applied: four drops were evenly distributed, after it had been stirred for two minutes. Afterwards it was left to

[5]Thanks to Morten Canth Hels for performing steps 1-4 and letting me be observing the process.

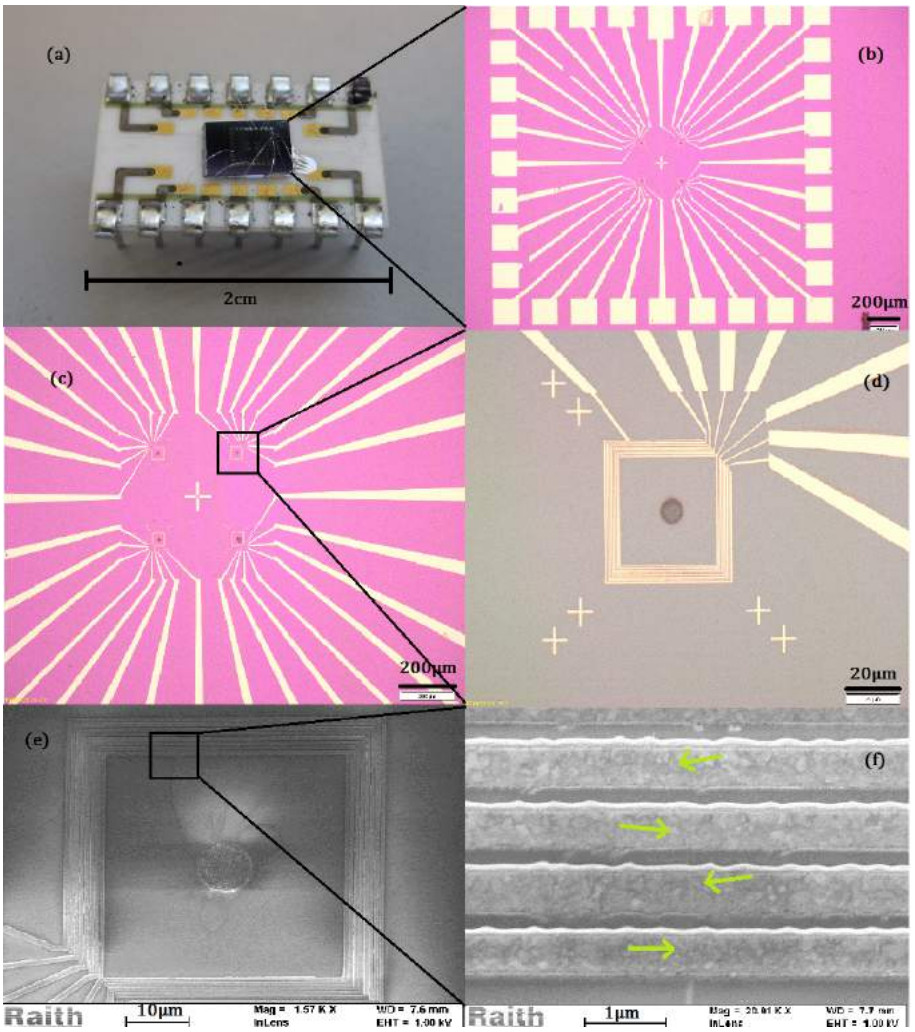

Figure 7: The sample: (a) The is sample glued to the chip carrier to connect to macroscopic equipment. The silver paint is conducting and connects the backgate, whereas the aluminum wires are bonded to the contacts. (b) A cell from the sample, imaged by an optical microscope. (c) A zoom of the cell, which reveals the four squares contained in each cell. (d) A further zoom of one of the squares. The catalyst island is the dot in the middle. The contacts are the squares surrounding the island, separated by 300nm. (e) Scanning electron microscope (SEM) image of metal contacts and catalyst after growth. (f) A tube suspended over multiple contacts (indicated by green arrows). The tube is difficult to see when suspended, and easier to see when it is bound to the substrate, due to charging of the substrate. Notice the irregular and melted contacts. Images were always taken after measurements, or of samples that were not to be cooled down to prevent damage by SEM.

dry completely, for approximately 11 minutes under a beaker, and it was then baked for seven minutes at 185 °C. Lift-off was executed in NMP (N-Methyl-2-pyrrolidone) at 76 °C, achieved by water-bath for two hours. The sample was then flushed with NMP to remove residual catalyst. The lift-off was checked under optical microscope. The last steps can be preformed again until lift-off is satisfactory, but this was not an issue during this project.

4.3 Growth of CNT in CVD Oven

CNTs can be obtained by different techniques: laser ablation, arc discharge and CVD. These techniques have different advantages, and as stated, the CVD furnace was used in this project[21].
As in applying the catalyst, the procedure can be done in a number of ways, which will give different results. The 'recipe' used consistently throughout this work has previously given good results, and is as follows:

- Place the sample in the 'boat' and insert in furnace[6].
- Start the oven with a setpoint of $T_{set} = 910\,^{\circ}\mathrm{C}$. To flush the chamber, set the gas flow of argon to 105% (Ar, 2L/min) for approximately five minutes.
- Decrease the flow of argon to 40%.
- When T_{set} is reached, turn off the argon and set hydrogen to 20% (H_2, 0.5L/min) for 10 minutes.
- In addition, turn on the methane to 13% (CH_4, 5L/min) for 20 minutes.
- Turn off the furnace, and stop the gas flow of hydrogen and methane. Set argon to 40% under the cool down. Turn on nitrogen gas for cool down to occur faster.

Two images are shown in Fig.7.(e)-(f) of samples after growth[7]. Melted and irregular contacts causing multiple QDs or possible shorts can be seen, confirming the harsh environment under growth. Usually the trench was reduced to approximately 100-200nm. Due to renovation of the institute, the CVD furnace was moved and this could have caused changes in the growth conditions. All generation except gen4 was grown before the move. Gen4 did indeed show signs of tubes, and others in the research group had no problems depositioning of tubes, so this was not taken as a disturbing factor.

4.4 Bonding to Chip Carrier

Lastly, to measure the QD behavior of a CNT, and thus the electronic structure, the samples need to be connected to macroscopic equipment. This is done by bonding the localized devices to a chipcarrier (localization of suspended tubes see Section5.1). The sample is glued to the carrier with conducting silver paint, which also connects the doped Si++ layer to a carrier pad. The wanted devices are bonded with thin aluminum wire to the pads, see Fig.7.(a).
The force with which the bonding takes place can be adjusted, and one has to be

[6]The orientation of sample relative to gas flow was the same at all growths.
[7]For additional SET images see Appendix C.

careful not to bond through the metal layers down to the conducting Si++ layer, or just scraping the metal, which was a problem for gen4.

4.5 Generation Development

Before presenting the different device generations it shall be noted that a number of tests were ran before the actual samples were made as in Fig.7, in order to save time and resources. Table.1 represents the major differences for the generations and their immediate outcomes. Notice that the thickness of Ta/W layers could not be determined, since it was done by sputtering.

Name	Contacts	Conclusions	Working devices
gen1	Ta/Pt	Residual resist made shorts.	12/224
gen2	Ta/Pt	Blurred metal contacts.	0/224
gen3	Ta/Pt	Well-defined contacts.	17/224
gen4	SiO_2/W/Pt	Metal shorts, and pealing.	4/224

Table 1: Table of generations. Working devices are exclusive metallic characteristics, since these were hard to distinguish from shorts.

Gen1

Ta and Pt (30nm). Originally Ta was chosen to get superconducting contacts (through proximity effect) for possible later application for Cooper splitter devices. After growth the contacts changed properties, which may have been caused by alloying effects at the high temperatures, and they also became less conducting. No superconducting effects were present in this project.
Probing at room temperature before growth indicated several shorts, most likely caused by residual resist (we attempted to remove the resist by sonacating and ashing, with no results). After growth, 12 obvious devices were present out of 224 contact combinations. Due to the shorts by resist and possible additional shorts by melted contacts, a great quantity of what resembled metallic tubes were also to be found (with G ranging from 0.12-1.1$\frac{e^2}{h}$). From a statistical perspective, metallic tubes are only to occur at every third tube[1], which supports the prediction of shorts. However, some of these may be true metallic tubes, or several suspended tubes. It was hard to distinguish the actual tubes from shorts.
Four of these devices were cooled down with samples used in the course Nano3, but because of the limited ports in the cryostat the chip carrier was soldered on top of another chip carrier, which destroyed all the clean devices. This could either be caused by discharging events, or simply by the heating while soldering(see Appendix C).

Gen2

I made use of the same metal combination that was used for gen1, but with different exposure parameters to prevent the residual resist shorts. This resulted in even

blurrier contacts, generating even more shorts (see Appendix C). This generation was not taken any further.

Gen3

Again, I used the same metal stacking, but with original metal sputtering. This generated well-defined contacts, with nearly no shorts before growth. This generation gave 17 obvious tubes (narrow gap and semiconducting). The number of resembling metallic tubes was drastically reduced, indicating less shorts by melted contacts or less multiple suspended tubes. Again, it was hard to distinguish the shorts from true metallic tubes. After growth there was no great change in conductance.
Multiple of these devices were taken for cool down. None of the cooled samples showed true metallic behavior. Some devices changed characteristics after loaded in the cryostat, indicating damage, discharging event or problem caused by severe bonding.
The measurements of these devices indicated no ultra clean devices (to be discussed in section.6.).

Gen4

Since no obvious clean devices were obtained, the attention was turned to previous work of clean devices made by H. O. H. Churchill ([5]). First a 50nm layer of SiO_2, a sticking layer of W (again undefined thickness) and an adhesion layer of Pt (30nm). To prevent shorts by melted contacts the sticking layer is a combination of W and SiO_2, with less metal to melt, but still achieving the wanted depth of the trench.
After the growth the sample had 4 detectable suspended tubes, and metallic characteristics at nearly all other contact combinations. These must be caused by melted contacts, residual resist or multiple multi-walled nanotubes generated by the W[5]. After the growth the metal contacts pealed off very easily, and the bonding process was rather difficult since the aluminum wire would not stick to the bonding pads (see Appendix C). Some of the few obtained devices was taken for cool down, and the measurements showed highly irregular structure.
For a short recap: it seems that gen3 had the greatest quantity and quality of tubes compared to the other generations. The reduction of shorts after growth could indicate more smooth and well-defined contacts compared to the other generations, which is an advantage in reducing unwanted multiple QDs. This sample is far from ideal since there are still a reduction in conductance, shorts and no superconductivity.

5 Experimental Setup

To observe the energy spectrum of the dot, and hence the clean CNTs, the criteria in Section.3.3 must be met. To do this, the measurements were done at cryogenic temperatures ($T < 1K$), but before cooling the sample, the tubes had to be located (with no use of electron microscopy to keep them as-grown). This was done at room temperature.

5.1 Setup at Room Temperature

Assuming well defined contacts, with no residual resist, no melted contacts and no backgate leak, the presence of conducting tubes can be assessed at room temperature simply through a $G - V_g$ characterization, with G as the linear conductance ($G = \frac{I}{V_{SD}}$) and V_g as the backgate.
This characterization was preformed on a probe station, in vacuum ($< 10^{-4}$mbar) to evaporate some of the contamination. With a constant DC bias voltage of 10mV across the contacts V_{SD}, G was plotted versus the backgate voltage V_g in the range [-20V; 20V], both forward and backward to check for hysteresis and reproducibility. Not only do these measurements locate the tubes, they also reveal what kind of tubes are suspended, e.g. semiconducting, narrow-gap or metallic. When adjusting V_g, the potential of the CNTs is adjusted, thus moving the bandgap relative to the Fermi energy. From eq.(4) only electrons in the range of k_BT are allowed to be excited, meaning that a bandgap energy relative to the temperature can be predicted.
All possible contacts were probed, and the curves resembling the ones predicted by theory[8] were bonded, and later cooled down.

5.2 Setup at Cryogenic Temperature

To achieve cryogenic temperatures an Oxford Instruments ^{3}He HelioxAC-V refrigerator was used[22]. When vacuum ($< 5 \times 10^{-5}$bar) is achieved in the outer vacuum chamber (OVC), the pulse tube cryocooler (PTC 2^{nd}) is turned on to cool down the system.
The sorption pump('sorb') needs to be cooled by PTC 2^{nd} to collect the He gas from the ^{3}He dump. To do this, the heat switch was turned on ($T_{switch} = 27$K) to make thermal contact. When the sorb is cooled ($T_{sorb} < 10$K) valve V1 is closed to prevent the He to diffuse back into the ^{3}He dump. The sorb was then heated to outgas the adsorbed ^{3}He, then I cooled down the ^{3}He pot to approximately the temperature of the PTC 2^{nd}. The V1 was opened, causing expansion of ^{3}He gas into the dump which lowered the temperature and caused liquid condensation of ^{3}He in the pot. To get the base temperature of ~ 300mK, the sorb was cooled which reduced the vapor pressure, resulting in the wanted temperature (see Fig.8).
The loaded sample was connected to an electrical circuit (see Fig.9(b)), which was controlled through MATLAB software.[9] The DAC's (digital to analog converter) and the ADC (analog to digital converter) were all connected to the DAQ (data acquisition), which again was connected to the software. The CNT was connected to a large resistor (10MΩ) and to a DAC in series. This DAC applies a voltage on the gate, and the resistor prevents any large currents through the tube, in case of backgate leak. To control the electrochemical potential of the drain contact μ_S another DAC is used. This DAC was connected to a voltage divider in order to heighten the resolution of the DAQ.[10] To the drain contact a current amplifier was

[8] See section2.2
[9] Software made by Anders Jellinggaard.
[10] The DAQ used is 16bit, in a 20V range, giving a resolution of $\frac{20V}{2^{16}} = 0.3$mV. But by the voltage divider, the rages becomes a factor of 500 smaller, giving a resolution of 0.305μV.

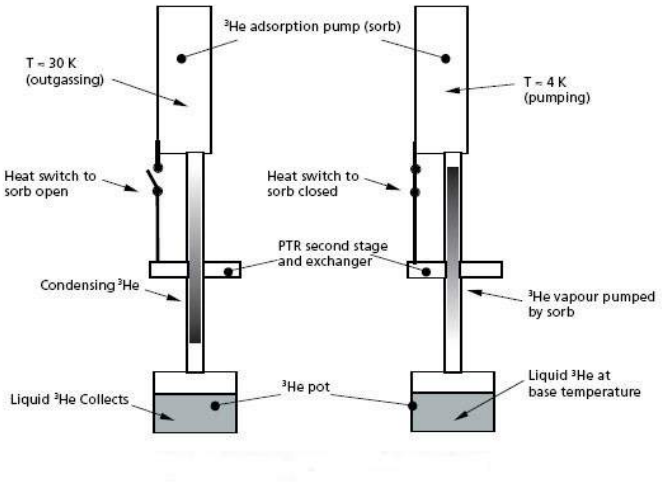

Figure 8: Schematic illustration of the cryostat, in the two cases of outgassing and at base temperature. The sorb, as explained in the text, are connected to a ^{3}He dump not shown in the diagram. The flow of ^{3}He can be controlled by valve V1 also not shown, from [23].

connected to amplify the small current through the device, but also to convert the current to a readable voltage for the ADC. Notice that the amplifier is grounded, hence grounding the drain contact, leaving the bias window controlled solely by the drain contact's electrochemical potential. Lastly, a lock-in amplifier was connected to the circuit to prevent noise, but also to measure the differential conductance ($\frac{dI}{dV_{SD}}$) instead of numerically calculate it for each data point[24][25]. The differential conductance are interesting due to the non-linear behavior of the dot.

6 Results and Interpretation

In this section the results from gen3 will be presented and discussed, since this sample gave the greatest quantity and quality of tubes. Furthermore, this generation had fewest shorts which could indicate smooth and well-defined contacts. A comparison of the other generations will be made throughout this section, in order to consider the advantages of different methods.

6.1 Room temperature and Energy Gap

In Fig.10. gate sweeps for different devices at room temperature are displayed. These sweeps reveal the type of tube suspended since metallic tubes do not have a energy gap, $E_g = 0$, thus the $G-I$-curve should be constant, as seen in Fig.10(c-d). Thermal excitations are contributing to the conductance, $E_g << k_BT$.
Semiconducting tubes, with a large energy gap, are predicted to totally suppress the conductance at a certain V_g, thus $E_g >> k_BT$. Seen from Fig10(b), the suppression takes place at $V_G \sim 0V$ for the forward sweep, and -15V for the backward. No conduction by thermal excitation are present.

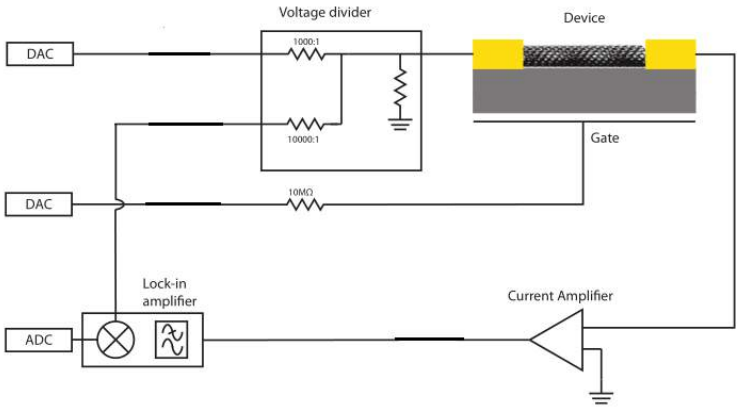

Figure 9: Schematic illustration of the electric setup with all the different components, explained in the text. The device obtained in this work is suspended, which is not the case in the figure. Edited from [26].

The third kind of tubes, narrow gap, only partially suppress the conductance at a small voltage range(-10V to 10V in Fig.10(a)),and therefore must have $E_g \sim k_B T$. The metallic tubes are not necessarily true metallic tubes ($E_{gap} = 0eV$), since very small band gap semiconducting tubes will show the same characterization. To be fully correct these should be defined as quasi-metallic henceforth.
Notice the relative difference in conductance for the different tubes. This is due to the Schottky barrier, which generates a greater electrostatic potential for tubes with greater energy gaps. For a description of the Schottky Barrier see Appendix.B, or [4].
I have also showed a gatesweep for gen4, which resembles a metallic tube. The conductance, however, is very high compared to the $4\frac{e^2}{h}$ predicted by theory, assuming one suspended tube. This either indicates multiple suspended tubes or shorts by melted contacts. From [5], it could also be multiwalled nanotubes generated by the Tungsten. A great quantity of similar results was obtained for nearly all contact combinations, ranging $1.5 - 5\frac{e^2}{h}$. Some of these could be metallic, but due to the small naturally abundance ($\sim 1\%$[4]), these were not taken further to the cryostat.

6.2 Coulomb Blockade

A gate sweep at base temperature is shown in Fig.11, for device A (top left in Fig.10). Here the energy gap is visible in the range 5V to 10V, with the hole regime for $V_g < 5V$ and electron regime for $V_g > 10V$ in agreement with the sweep at room temperature. There is a relative difference in conductance for the two regimes, most likely caused by the Schottky barrier (See Appendix.B). For CB to occur, the criteria given in Section.3.3 have to be met. This is not the case in the hole regime, since the conductance is comparable to the conductance quantum ($\frac{e^2}{h}$), which gives an open dot. This can also be seen from Fig.11, where what appears to be Fabry-Pérot oscillations are dominant[19]. Since the energy characterizations are easiest obtained through CB, this segment will be considered first ($V_g > 10V$).

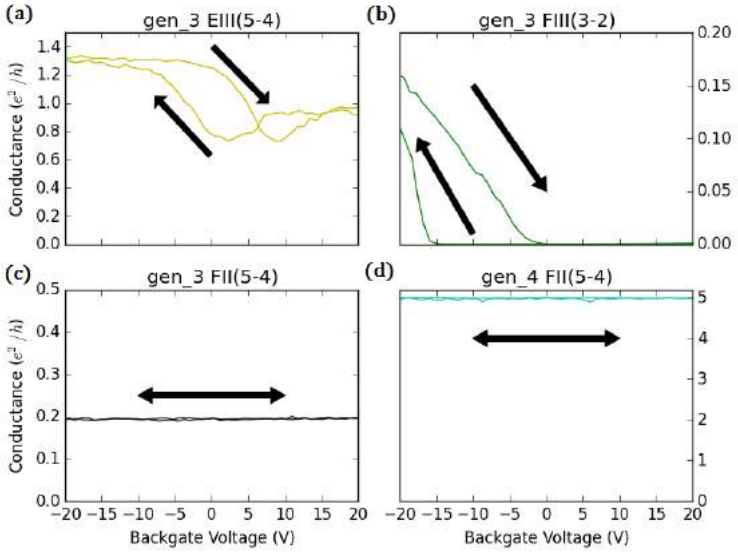

Figure 10: Characterization at room temperature: (a) Narrow gap tube, generated by strain of tubes. (b) Semiconducting nanotube, resembles field-effect transistor (p-type). (c) Metallic tube. These were hard to distinguish, since shorts likewise will be independent of the gate voltage. (d) Expected short due to the high conductance, or multiple suspended tubes.

The inset of Fig.11. is a zoom of the CB regime to be considered. From Section.3.2 it is then clear that the peaks are positions with SET, whereas the valleys are CB. Going from one valley to another the number of electrons on the dot are increased by one as indicated. Thus, there must be a relation between the difference in gate voltage between two peaks and the addition energy:

$$\Delta V_g = \frac{e}{C_g} + \frac{\Delta E}{e\alpha}. \tag{15}$$

Derived from eq.(8) and eq.(10), assumed that the number of electrons on the dot are greater than one. Here $\alpha = \frac{C_g}{C}$ is the lever arm, describing the coupling to the backgate, and ΔV_g is the change in gate voltage for adjacent peaks. For further determination of the energy levels, we need to find the different capacitors through the bias sweep. Notice that the last term in eq.(15) is equal to zero for degenerate states.

6.3 Shell Structure

Shell structure is a way of describing the levels of the quantum dot, again in analogy with an atom. One level (shell) for a perfect tube is four times degenerated because of valley quantum number and spin. It will then be expected that the cost of adding the N'th electron to the dot would be $E_C + E_{add}$, as earlier stated. But, for the next three electrons it should only cost the charging energy E_C. This should be manifested in both the gatesweep, with one big valley followed by three small, and in the bias sweep, with one big diamond followed by three small.

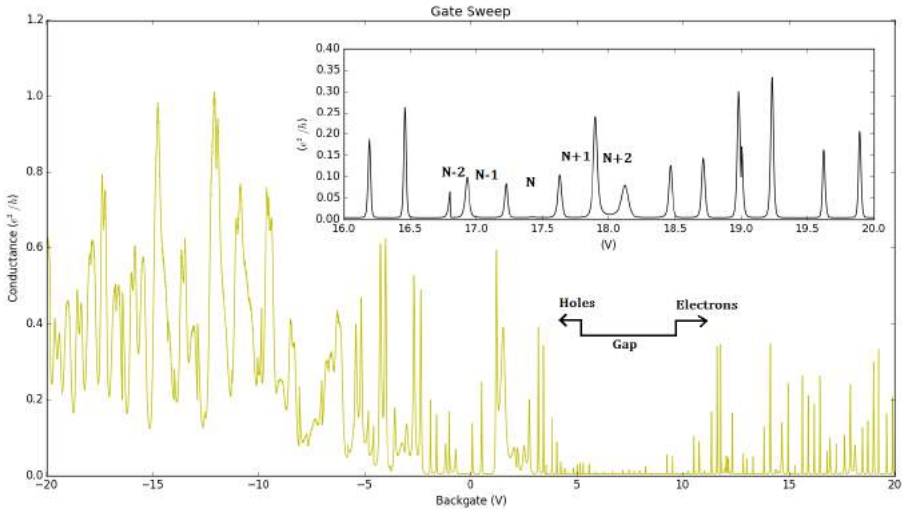

Figure 11: Gate sweep: Main: Gate sweep for device A. Gap, hole and electron regime is indicated in the figure, in agreement with the measurements at room temperature. CB only takes place in the electron regime due to the high conductance at hole regime. Inset: A zoom of the CB-regime. Here are the number of electrons on the dot indicated.

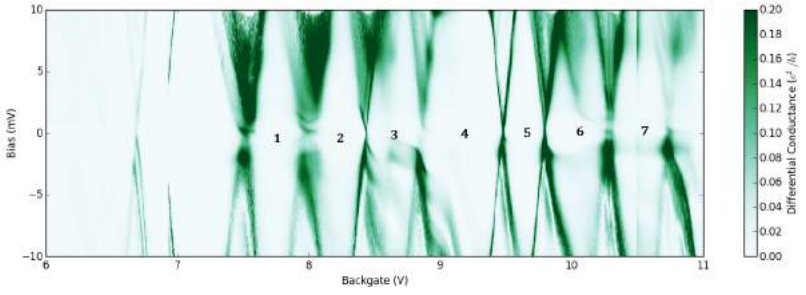

Figure 12: A bias sweep for CB regime. The numbers in the figure are just numeration of the diamonds, and should not be understood as the number of electrons on the dot. Green indicates conductance, whereas white is blockade.

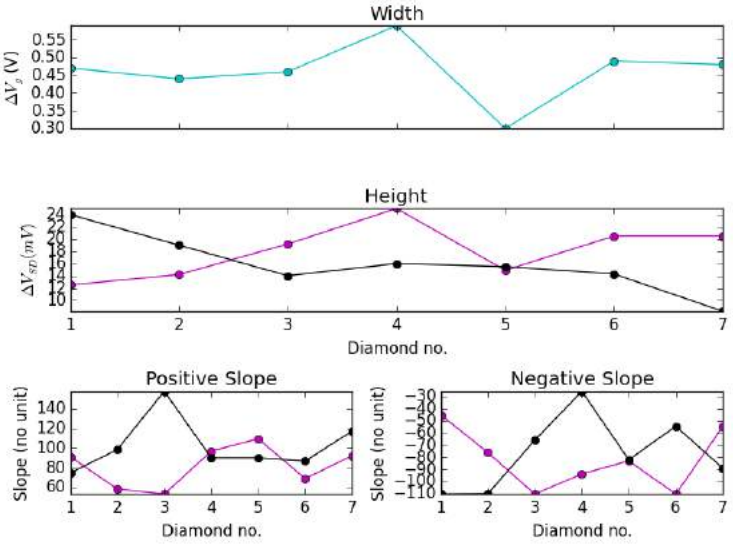

Figure 13: Plots of width, height and slopes from Fig12. It is clear from these plots that no regular structure is to be found. Due to asymmetry for negative and positive bias both of these are plotted. Here purple is for positive bias, and black for negative bias.

For an overview of the tube structure, the width, height and slopes from Fig.12, see Fig.13. Due to asymmetry for positive and negative bias, the slopes and heights are read off for both regimes.

It is clear that no periodic structure is to be found in the plots, hence no shell structure or spin degenerated states. The asymmetry of the bias regimes and the great fluctuations for the slopes are quiet remarkable.

For further characterization, it will be assumed that spin degeneracy is present for diamond 3 to 6 in the positive bias regime. This is a rough assumption, but a must in order to obtain the energies. Using the data from Fig.13 gives the charging energy $E_C \approx 17meV$, gate coupling $\alpha \approx 0.45$ and the quantum level spacing $\Delta E \approx 71meV$, all relative high[4][20]. Furthermore the energy gap was found to be $E_g \approx 2.25eV$, which is also rather high, since the energy gap should be the same order of magnitude as the room temperature ($k_BT \sim 26meV$).

To reveal the suspension of the CNT, and the geometry of the contacts, a simple estimate can be done:

$$E_C = \frac{e^2}{C} \approx \frac{e^2}{\epsilon_0 \epsilon_r L} \tag{16}$$

$$\Downarrow$$

$$L = \frac{e^2}{\epsilon_0 \epsilon_r E_C} \approx 1.06\mu m, \tag{17}$$

assumed that the tube is fully suspended, without touching the substrate ($\epsilon_r = 1$). From Section.4. it is clear that this is incorrect, since the geometry of the trench was 300nm, and will only decrease in case of melted contacts.

All these unpredicted high values advocate an ill-defined dot, either caused by irreg-

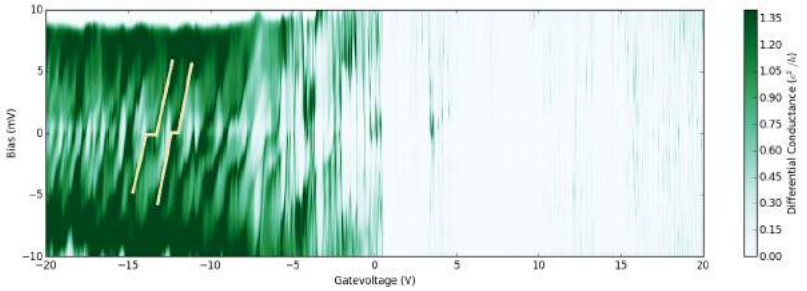

Figure 14: The full bias spectrum. Reaviling higher conductance for negative bias, as predicted and seen at room temperature. This higher conductance shows a new phenomena for open dots; Kondo Physics. The beige lines indicate the stair-like structure of stronger couplings.

ular metal contacts, defects in the CNT, multiple interacting QDs or some unknown phenomena.

6.4 Kondo Physics

So far only closed QD has been considered, but in the p-regime it is clear that this is not the case, see Fig.14. From the gate sweep at base temperature, what appeared to be Fabry-Pérot oscillations, are here shown to be the phenomena of Kondo physics. Originally known from the resistance characterizations of metal alloys containing magnetic impurities, where suddenly the resistance raise as $log(T)$, at a very low temperature (T_K)[13].
As for most transport properties in CNTs it is convenient to consider the potential landscape, Fig.15(a). Here, due to many body phenomena, a new level is produced and current can flow, where CB normally would be the case. Notice that an odd number of electrons must be present on the dot, since an unpaired spin has to be present. This means that only every second diamond would show conductance (Fig.15(b)). This periodicity can also be seen in the zoom of the bias sweep, with every second diamond showing conductance (Fig.15(d)).
The Kondo effect only takes place below the critical Kondo temperature T_K, typically ranging from 1-10K. Above this temperature CB should be visible [10][11]. To see this transition, a gate sweep was preformed multiple times at a Kondo resonance to check for major hysteresis change. Afterwards, the gate sweep was preformed at various temperatures, as seen in Fig.15(c). The relative broad Kondo peaks are expected to split up into Coulomb oscillations (peaks with electron transport, and valley with suppressed conductance). As seen in the figure, it seems that the peaks are broadened instead of dividing. This broadening seems more like a temperature smearing of the levels and not Coulomb peaks. This is also supported by the reduction in conduction, which is characteristic for higher temperatures.
The Kondo temperature can be estimated through the broadness of the new conduction states in the diamonds, and was estimated to $T_K \sim 10K$. To get a better analysis of the Kondo effect the cryostat should have been heated to at least 10K, but due to problems while heating, this was not possible. However, to conclude anything

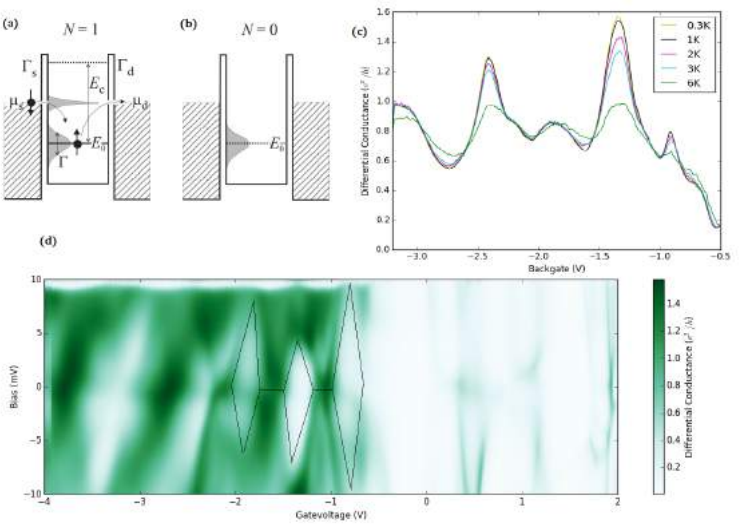

Figure 15: Kondo effect: (a) Schematic illustration of Kondo effects. Notice that this phenomenon only takes place when an unpaired electron is present on the dot. Whereas in (b) where no Kondo state is produced, from [13]. (c) Temperature dependency of Kondo peaks. (d) Zoom of bias sweep. Here the black lines indicate the CB diamonds, and the horizontal lines the new conducting states. Here is the periodicity of unpaired electrons present.

about this extra feature, it seems to confirm the irregular electronic structure of the CNT, which generates new complicated resonance phenomena.
Furthermore it is clear that the coupling ($\Gamma = \Gamma_S + \Gamma_D$) in this regime is better due to the smaller Schottky. But an interesting feature is also visible: the relative stronger coupling of the positive slopes in the diamonds, and the Kondo states, seem to make stair-like structures of higher conductance (marked with beige lines in Fig.14). Through the potential landscapes it can be shown that this structure is due to a stronger coupling to the source contact, which confirms the irregularity of the contacts.

7 Conclusion and Outlook

It turned out to be a far more circumstantial procedure to fabricate ultra-clean suspended as-grown tubes, than first assumed. The harsh environment during growth in the CVD furnace caused drastic changes of the predefined contacts. These includes melting, irregularities and alloying (preventing superconducting effects.).
Different generations were made to met these harsh conditions. In the end, it was clear that gen3 had the greatest quantity and quality of tubes. One of these devices' results were presented showing a highly irregular electronic structure and high energies compared to literature, either caused by multiple interacting QDs, impurities in the tubes or by an other unknown phenomena. This sample also showed Kondo effects and varying couplings.

To make a comparison to normally obtained devices, it seems that the original procedure paradoxically generates cleaner tubes. However, in my study the quantity of devices seems greater, and easier to obtain, since there is no need of alignment of contacts or etching.
For further investigation the main focus should be on the fabrication steps. New metal stacking could optimize the contacts, or one could simply try a norther geometry. When confining the CNT as a QD, the trenches can be up to a couple of micrometers wide[4], and therefore the geometries could be defined with wider trenches, probably giving less shorts and better defined contacts. If the quantity of tubes are to be optimized, the area of catalyst island could be increased which would increase the probability of suspended tubes. In addition, the metal stacking could be optimized in the manner as [5], with a sticking layer that does not melt (SiO_2, melting point: 1,986K).
Finally, it could be interesting to bake the predefined contacts at 910 °C(without deposition tubes), and thereafter mechanically transfer a well defined tube to the contacts[3][27]. This could give an insight into the irregularity of the contacts, which seemed to be the main challenge during this project. Additionally, the research could be taken further be applying a magnetic field to reveal valley magnetic moment and spin-orbit couplings, but also to investigate the Kondo effect further.

8 Acknowledgments

I want to thank Morten Canth Hels and Kasper Grove-Rasmussen for the endless discussions and questions during this project. I would also like to thank Jesper Nygård for making this project possible, and for leading me in the right direction during my work. I am thankful to these three men for introducing me to the fascinating world of mesoscopic physics, through the course Nano3 and through this project.
Lastly, I am forever indebted to the QDev espresso machine, as it has been of great help to me for these past few months.

9 Appendix

Appendix A: Current Annealing

Nanoelectronic and Mesoscopic Physics Group at the University of Basel produce clean CNT on ferromagnetic Py contacts. Py oxidize easily and generates an insulating oxide layer between the tube and the contact. A reduction of this high resistance can be obtained by applying a high voltage over the sample, which generates an irreversible dielectric breakdown. For setup and results see[3].
The same procedure was done on the clean devices with high resistance to see if any contaminating layer had been generated on the Pt contacts (this should not be the case since Pt is an noble metal.). The annealing did not change any characteristics of these devices.
Next it was done on device A to see if the annealing could remove irregularities and impurities, with no results.
Applying a too high voltage can damage the device, so the annealing steps are normally done with a small increase in voltage. But since all measurements necessary for this thesis already were performed, this was not a concern, and a high voltage was applied (∼5.5V). Yet still no change was observable, except from device A. After the severe annealing the p-type narrow gap tube was all of a sudden n-type, with lower conductance (Fig.16). This procedure has shown great results for oxidized ferromagnet contacts, but it is clear that this procedure did nothing constructive for the devices in this thesis.

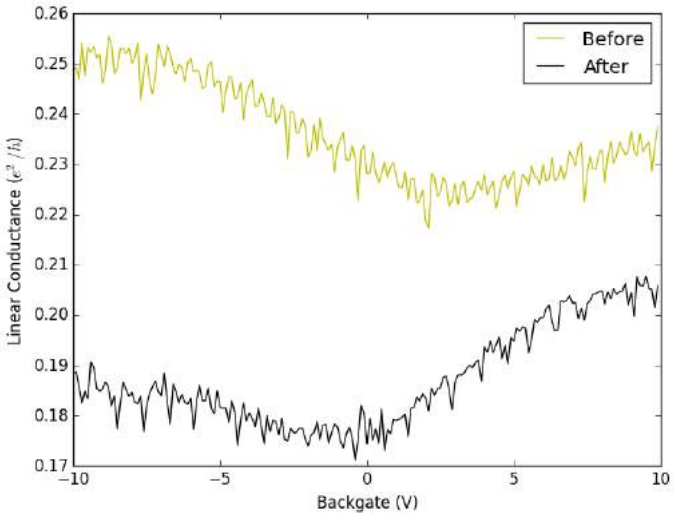

Figure 16: Gate sweep of Device A before and after current annealing. Showing the unexpected reduction in conductance, and change from p- to n-type.

Appendix B: Schottky Barrier

As for the theory of pn-junctions; when two different materials are sandwiched together, there must be an alignment of the Fermi levels, causing a spilling of electrons

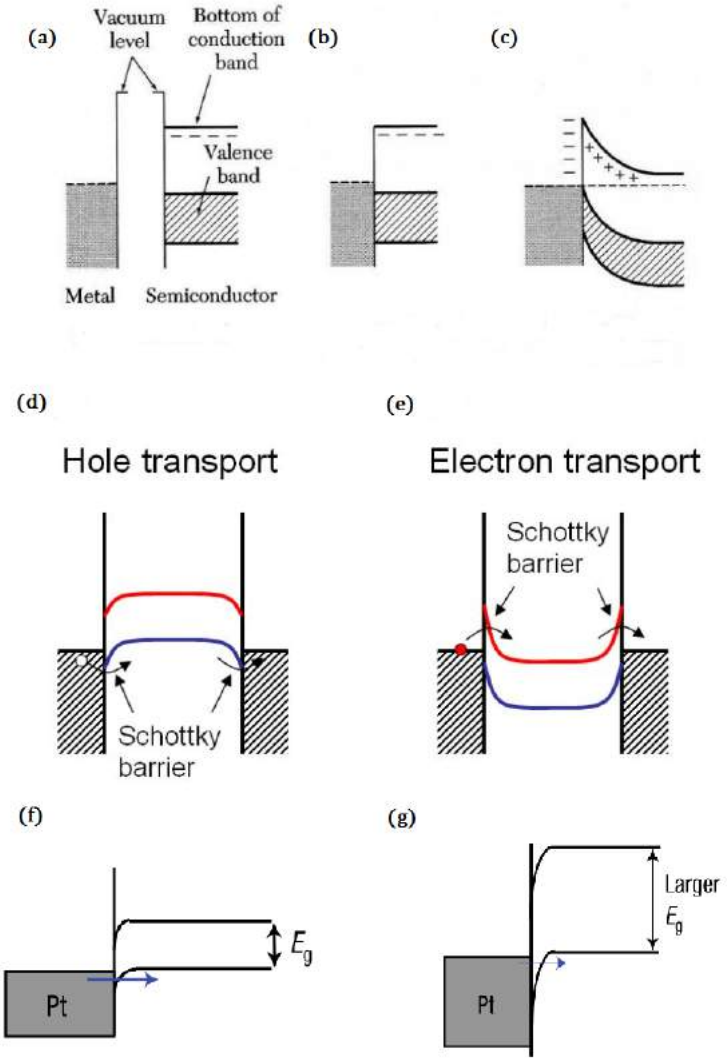

Figure 17: Schottky barrier: (a)-(c) Barrier between metal and semiconductor. Electrons from the semiconductor transfer to conducting band of the metal generating a static potential,[14]. (d)-(e): Schematic diagram of transport in conduction band and valence band, which explains the difference of conductance in the two regimes, [11]. (f)-(g) Explanation of difference in conductance of different tubes, since a greater energy gap gives a higher barrier, [4].

(holes). This spilling introduces an electrostatic potential and hence a energy barrier for the electrons(holes), generating a resistance at the interface, see Fig.17.(a)-(c). Semiconducting tubes have the greatest E_g, and must therefore produce a greater Schottky barrier compared to narrow gap- and quasi metallic tubes. The small energy gaps reduce the bending of the bands, which explains the relative difference in G of the different kind of tubes, again see fig.17.(f)-(g).
Lastly, from the theory of holes the conduction in p-regime takes place in the valence band, and the conduction band in n-regime. In Fig.17.(d)-(e) it is clear that the

Schottky barrier is smaller in p-regime and larger in n-regime, generating the relative difference in conductance for the two regimes. In agreement with Pb- and Pt contacts in previous studies[11][5][4].

Appendix C: Imaging

In this section images of devices will be presented. In order to keep the CNTs as-grown all images taken by SET were taken after measurements, or on imperfect devices. This section will confirm suspended tubes, and irregular contacts due to the harsh environment during growth. Notice that no SET images of gen4 is presented due to the limited amount of time.

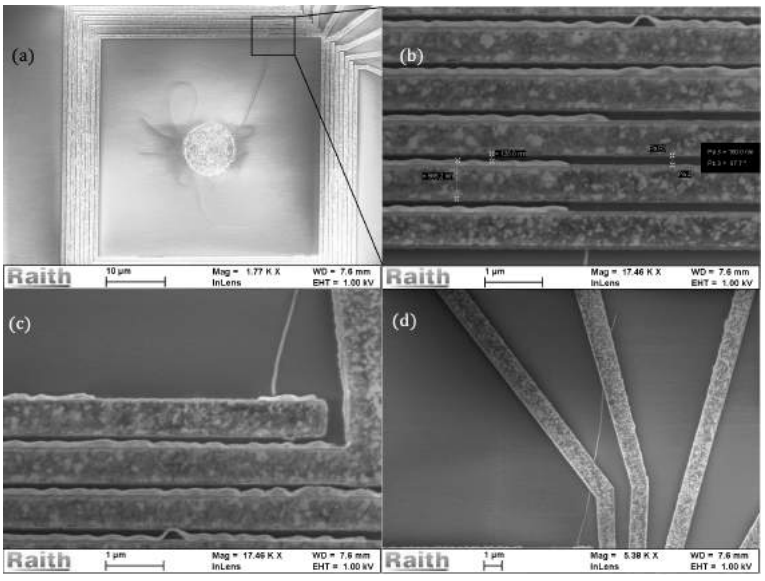

Figure 18: SET images of gen1. Here multiple tubes are grown from the catalyst dot, but only one suspended, as wanted(a). The suspended tube stretches several micrometers, as seen in (b)-(d), onto the metal connecting the contacts, disturbing the wanted electric circuit. These images are also interesting in the way that the irregularity of the contacts are visible. Some lengths are giving in (b), which shows the decrease of the width of the trench. Suspended tubes are not as visible as tubes on the substrate, due to charging of the substrate [5].

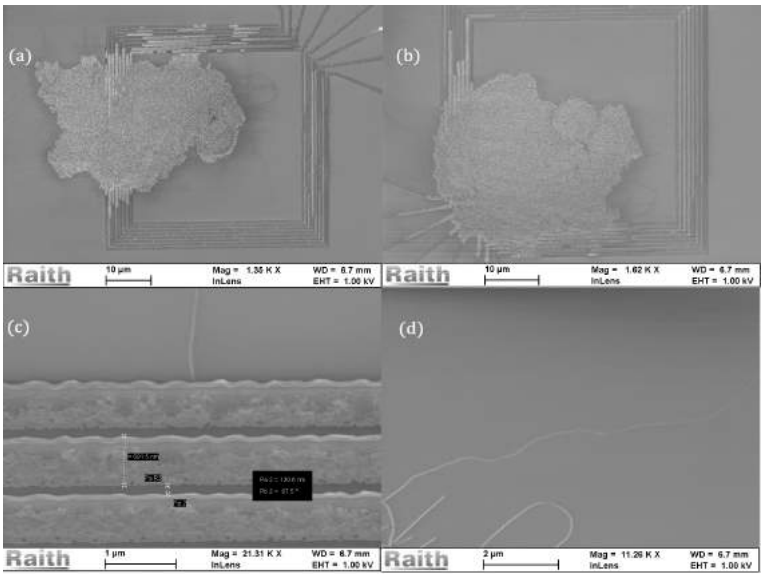

Figure 19: SET images of gen1, but with other cases of possible disturbance in the measurements. In (a)-(b) the catalyst is somehow smeared onto the metal contacts. This is often not a surprise, since it is often visible by optical microscope when applying the catalyst. In (c) the tube is cracked, thus not suspended. (d) illustrates a very kinked tube, often generating irregular structure.

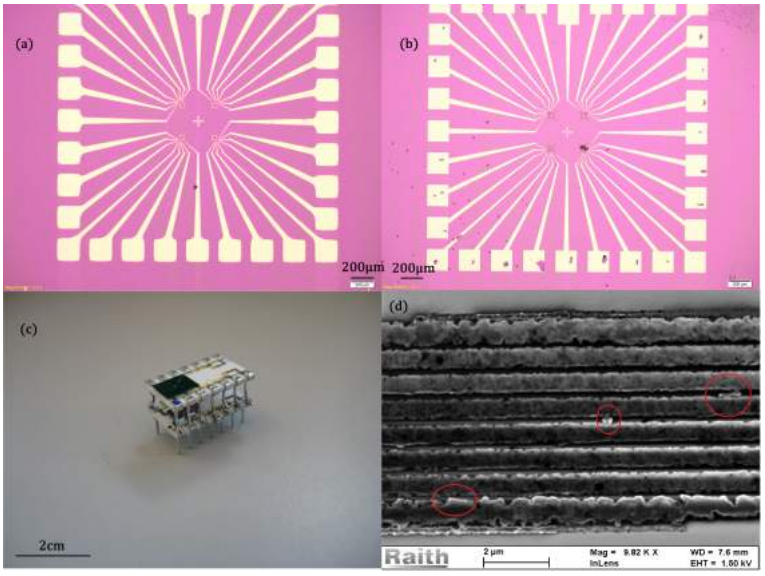

Figure 20: Additional images:(a) is a image obtained by optical microscopy of the metal geometry of gen2. Here the blurred unsharp features are clear, generating extra shorts. (b) gen4 with scrapped metal pads after probing at room temperature. Notice that smearing of catalyst is visible in down right square. (c) A sample from gen1 soldered on top of a sample used in the course Nano3. (d) an exemplary SET image of highly irregular contacts (gen3). The red circles indicate spots of possible shorts.

References

[1] J. Appenzeller *et al.*, *Carbon Nanotubes for Data Processing*, chap. 19, in Nanoelectronics and Information Technology, R. Waser (ed.), Wiley-VCH Verlag GmbH & Co. KGaA. 2003.

[2] J. Nygård, & D. H. Cobden, *Quantum Dots in Suspended Single-wall Carbon Nanotubes*, Applied Physics Letters, **79**, p.4216-4218, 2001.

[3] J. Gramich, *et. al.*, *Fork Stamping of Pristine Carbon Nanotubes onto Ferromagnetic Contacts for Spin-valve Devices*, 2015.

[4] J. Cao *et al.*, *Electron Transport in Very Clean, As-grown Suspended Carbon Nanotube*, Nature Materials, **4**, p.745-749, 2005.

[5] H. O. H. Churchill, *Quantum Dots in Gated Nanowires and Nanotubes*, Ph.D. Thesis, 2012.

[6] M. P. Pedersen, *Fabrication and Characterization of As-grown, Suspended Single-Walled Carbon Nanotubes*, Bachelor Thesis, 2013.

[7] J. Fülöp, *et al.*, *Local Electronic Tuning of the Nonlocal Signals in a Cooper Pair Splitter*, Physical Review B, **90**, p.235412, 2014.

[8] D. J. Griffiths, *Introduction to Quantum Mechanics*, Pearson Education Limited, 2014.

[9] P. Hedegaard, *Statistisk Fysik*, Polyteknisk Boghandel, 2015.

[10] E. A. Laird et al., *Quantum Transport In Carbon Nanotubes*, from Cornell University Library, http://arxiv.org/abs/1403.6113, 2014.

[11] K. Grove-Rasmussen, *Electronic Transport in Single Wall Carbon Nanotubes*, Ph.D. Thesis, 2006.

[12] A. H. Castro Neto et al., *The Electronic Properties of Graphene*, in Reviews of Modern Physics, **81**, p. 109-162, 2009.

[13] J. Nygaard, *Experiments on Mesoscopic Electron Transport in Carbon Nanotubes*, Ph.D. Thesis, 2000.

[14] C. Kittel, *Introduction to Solid State Physics*, John Wiley & Sons, Inc, 2005.

[15] J. Solyom, *Fundamentals of the Physics of Solids*, Volume II, chapter 16, Springer-verlag Berlin And Heidelberg Gmbh & Co. Kg, 2010.

[16] S. Datta, *Electronic Transport in Mesoscopic Systems*, Cambridge University Press, 1995.

[17] L. P. Kouwenhoven and P. L. McEuen, *Single Electron Transport Through a Quantum Dot*, in Nanotechnology, G. Timp (ed.), Springer, 1999.

[18] R. Hanson *et. al.*, *The Constant Interaction Model*, Rev. Mod. Phys. **79**, 2007.

[19] T. Ihn, *Semiconductor Nanostructures, Quantum States and Electronic Transport*, Oxford University Press, 2010.

[20] S. Sapmaz, *et. al.*, *Quantum Dots in Carbon Nanotubes*, Semiconductor Science and Tecnology, **21**, p.52-63 2006.

[21] J. Kong *et. al.*, *Synthesis of Individual Single-walled Carbon Nanotubes on Patterned Silicon Wafers*, Nature, **395**, p.878-881, 1998.

[22] Oxford Instruments, *HelioxAC-V ^{3}He Refrigerator System Manual*, Tech.rep., 2007.

[23] Oxford Instruments, *Description* from http://www.oxford-

instruments.jp/products/cryogenic-systems/helium-3-refrigerators-300mk/cryogen-free-helium-3-refrigerators/cryogen-free-helium-3-refrigerator-helioxac-v, 2015/05/08.

[24] *About Lock-In Amplifiers*, Stanford Research Systems, Application note no. 3.

[25] M. C. Hels, *How Do Lock-in Measurements Work?*, notes from the course Nano3: Kvantefænomener i Nanosystemer, 2015.

[26] S. Maibom, *Carbon Nanotube Quantum Dot with Superconducting Electrodes*, Bachelor Thesis, 2010.

[27] F. Pei *et. al.*, *Valley-spin Blockade and Spin Resonance in Carbon Nanotubes*, Nature Nanotechnology, **7**, p.630-634, 2012.